# IMPLEMENTING FEEDBACK CONTROL ON A NOVEL PROXIMITY OPERATIONS SIMULATION PLATFORM

A Thesis

by

KURT DALE AURES-CAVALIERI

Submitted to the Office of Graduate Studies of
Texas A&M University
in partial fulfillment of the requirements for the degree of

MASTER OF SCIENCE

May 2011

Major Subject: Aerospace Engineering

# IMPLEMENTING FEEDBACK CONTROL ON A NOVEL PROXIMITY OPERATIONS SIMULATION PLATFORM

A Thesis

by

KURT DALE AURES-CAVALIERI

Submitted to the Office of Graduate Studies of
Texas A&M University
in partial fulfillment of the requirements for the degree of

MASTER OF SCIENCE

Approved by:

| | |
|---|---|
| Co-Chairs of Committee, | John E. Hurtado |
| | John L. Junkins |
| Committee Members, | Shankar P. Bhattacharyya |
| Head of Department, | Dimitris C. Lagoudas |

May 2011

Major Subject: Aerospace Engineering

# ABSTRACT

Implementing Feedback Control on a Novel

Proximity Operations Simulation Platform. (May 2011)

Kurt Dale Aures-Cavalieri, B.S., The State University of New York at Buffalo

Co–Chairs of Advisory Committee: Dr. John E. Hurtado
Dr. John L. Junkins

Recently, The Land, Air and Space Robotics (LASR) Laboratory has demonstrated a state-of-the-art proximity operations test bed that will revolutionize the concept of portable space systems simulation. The Holonomic Omni-directional Motion Emulation Robot (HOMER) permits infinite, un-tethered circumnavigations of one object by another. To allow this platform to operate at the desired performance, an appropriate implementation of feedback control is essential. The dynamic model is derived and presented using a Lagrangian approach. A Lyapunov method is used to form proportional-derivative (PD) and proportional-integral-derivative (PID) feedback controllers. These controllers are validated with computer-based simulation and compared through experimental results. Finally, a frequency analysis is performed in an effort to identify the bandwidth of the system and provide a better understanding of the expected system performance for reference motions containing harmonic perturbations.

To my grandfather, Richard J. Wohlfeil

# ACKNOWLEDGMENTS

I would like to extend my gratitude to my advisors, Drs. John E. Hurtado and John L. Junkins for their profound guidance, their continued support, and giving me the chance to reach my full potential. Additionally, I want to thank Jeremy Davis and James Doebbler for their assistance with this work and for taking me under their wings to help me grow as a researcher. Finally, I would like to thank my family and friends for their endless support.

TABLE OF CONTENTS

CHAPTER Page

# LIST OF TABLES

# LIST OF FIGURES

FIGURE Page

# CHAPTER I

## INTRODUCTION

Over the past six decades, extensive effort has led to ground-based simulation platforms for the development and verification of advanced space systems and their control algorithms. Several designs are currently in use ranging from air bearing tables to crane-like mechanisms, each with its own unique advantages and disadvantages.

One approach involves emulating key aspects of the space environment and using the actual hardware and actuators to achieve the dynamics. Whereas free-fall chambers or parabolic trajectory aircraft can be used to provide a short-term zero-g environment, the method usually used is to simulate contact-free zero-g motion along specific degrees-of-freedom (DOF) by reducing friction using air bearings [2]. Obviously, the short duration and release/capture complications limit the utility of this approach. The Synchronized Position Hold Engage and Reorient Experimental Satellites (SPHERES) project has made use of air bearings in the testing of an actual space-based micro satellite in a ground-based testbed [3]. Relative motion of 6-DOF micro-satellites has been ground tested in 3-DOF using a laboratory air bearing table and two of the SPHERES micro-satellites. For spacecraft reorientation dynamics and control, friction-free 3-DOF motion can be achieved using a spherical air bearing and using reaction wheels, control moment gyroscopes, or thrusters [4].

Another popular approach is to use robotic positioning hardware to emulate the dynamical motion of some virtual vehicle model. This is a hybrid approach where the dynamics of the subject vehicle are simulated numerically, and this simulated motion is tracked by a hardware platform. Using this approach, hardware items such as sen-

---

The journal model is *IEEE Transactions on Automatic Control*.

sors or docking mechanisms can be evaluated in realistic relative motion situations. One method of tracking the precision motion uses a parallel kinematics device, such as a Stewart platform, to provide high precision motion with good stiffness characteristics. However, these devices provide only limited ranges of 6-DOF motion due to the restricted workspace. Other approaches use an array of mobile carriages or gantries to allow for a larger workspace, supplemented with a robotic assembly that may allow for extra degrees-of-freedom.

For example, to test the performance of a sensor, Schaub et al. are using a single, untethered mobile wheeled robot to emulate the dynamics of a simulated vehicle relative to some target [5]. The Naval Research Laboratory's Proximity Operations Testbed at the Naval Center for Space Technology can simulate the relative motion of two large spacecraft using its dual motion platforms. Each platform uses a large 3-axis gantry crane augmented with a robotic arm to provide 6-DOF positioning of target and pursuer [6]. Similarly, NASA's Flight Robotics Facility at the Marshall Space Flight Center uses a combination of these methods by combining a 6-DOF air bearing robot on a flat floor with a large overhead gantry crane capable of positioning a payload in 6-DOF [7].

## A. HOMER

In contrast to those facilities, the Land, Air, and Space Robotics (LASR) Laboratory at Texas A&M University has recently developed and demonstrated a novel robotic platform designed specifically to overcome the limitations of current simulation hardware [8, 9]. The Holonomic Omni-directional Motion Emulation Robot, referred to as HOMER, consists of a mobile, planar base accompanied by a Stewart platform, shown in Fig. 1. Here, the term "holonomic" is used in a robotics sense where the

number of controllable degrees-of-freedom is equal to the total degrees-of-freedom of the robot. In a strict dynamics sense, the planar base is classified as a non-holonomic system because of the imposed no-sideslip constraints on six caster wheels, which will be discussed later. The base provides large, omni-directional 3-DOF planar motion, whereas the Stewart platform provides smaller motion in all 6-DOF to a high degree of precision. Not only does the Stewart platform superimpose out-of-plane motion, but it also can be used to "clean up" the less precise motion of the base. The mobile platform approach provides emulation capabilities similar to NRL's facility, though with a lower payload capacity but with several distinct advantages:

1. Allows for untethered circumnavigation of two or more vehicles.
2. Planar motion is limited only by the size of the workspace.
3. Low-cost alternative to larger installations while maintaining high fidelity.
4. Supports testing of non-spacecraft multi-vehicle systems, such as autonomous aerial refueling.
5. The entire facility is quasi-portable; in less than 24 hours, the system can be relocated as needed.

HOMER's base consists of a rigid main, three casters, and six drive wheels. Each caster is powered by two identical motor-wheel pairs making the 3-DOF base an over-actuated system. The unique, redundant drive wheels with off-set caster design (as seen in Fig. 2) enable each platform to rotate and translate independently, allowing a true, high fidelity simulation system ideal for satellite operations. From one point of view, the three casters could be viewed as three cooperating robots whose wheel motions are commanded to generate the required kinematic velocity or acceleration of their respective pivot points, compatible with the desired base motion. Only routinely

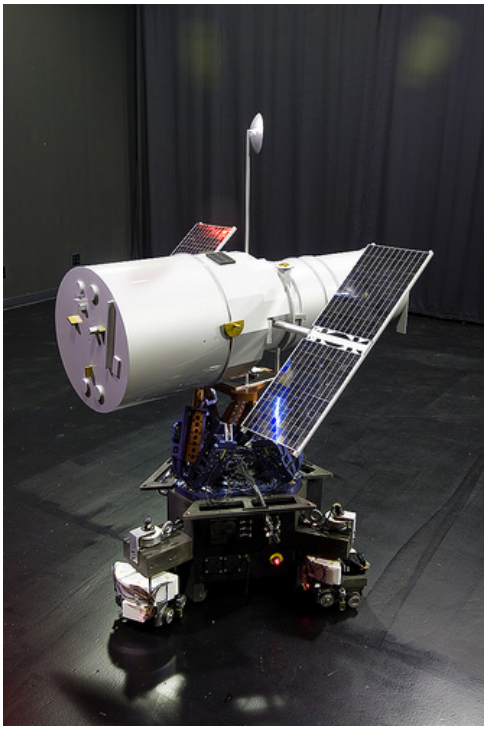

Fig. 1. HOMER with a 10:1 Scale Hubble Space Telescope [1]

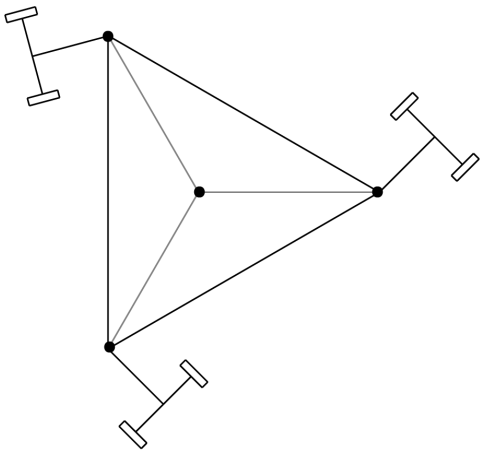

Fig. 2. Simplified Aerial View of HOMER's Base

flat floors are required because the redundant DOF platform can clean up a wide class of non-ideal departures and disturbances. HOMER's kinematic limits are summarized in Table I. While these values exceed specifications, they are experimentally derived.

Table I. HOMER's Kinematic Limits

| Property | Limit | Units |
|---|---|---|
| Velocity | 0.228 | $m/s$ |
| Acceleration | 0.0571 | $m/s^2$ |
| Angular Velocity | 0.596 | $rad/s$ |
| Angular Acceleration | 0.149 | $rad/s^2$ |

## B. Sensing Systems

The sensing systems at the LASR Laboratory, including Indoor GPS from Metris and VICON motion capture system, provide accurate position and orientation measurements of rigid bodies within the workspace. To allow the HOMER platform to operate at the desired performance, a proper implementation of feedback control is essential. The VICON high-speed camera system utilizes six high-speed cameras and passive retro-reflective markers. These synchronized 16 megapixel cameras run at a 120 Hz update rate with random errors at the one mm level. Fiber-optic cables convey the data from the VICON cameras to a dedicated processor. One to two millimeters of systematic error can be eliminated by calibration. At least four passive markers must be placed in a unique, rigid pattern that can then be tracked by the system software as a rigid body. The Indoor GPS system uses six rotating laser transmitters and four

sensors that are rigidly attached to the body of interest. This system runs at approximately 40 Hz and provides 0.5 mm inertial accuracy throughout the workspace. The combination of these sensing systems provide high precision measurements at a high update rate. Each of these systems has a semi-automatic self-calibration process that uses redundant multi-view measurements to accurately estimate the VICON cameras to each other and the Metris laser transmitters relative to each other. The Metris system establishes the laboratory coordinate system and calibration methods have been developed to locate the VICON frame in the Metris frame.

In the following pages, the equations of motion of the base will be presented along with multiple control laws paired with experimental results and the bandwidth capabilities of the base. Chapters II and III will derive the dynamic model and a proportional-derivative (PD) controller, respectively. Chapter IV validates the model and controller through computer-based simulation while studying the accuracy effects of possible modeling errors and known hardware difficulties. Chapter V contains experimental results obtained from the PD controller, then a new proportional-integral-derivative (PID) controller will be introduced in Chapter VI along with experimental results for comparison. Finally, a closed loop bandwidth study is presented in Chapter VII to highlight the effects of requested high frequency motion. Conclusions and future work can be found in Chapter VIII.

# CHAPTER II

## MODEL

The dynamic model derivation begins with the vector-matrix form of the Lagrangian equations of motion and the system of Pfaffian constraints [10].

$$\frac{d}{dt}\frac{\partial L}{\partial \dot{\mathbf{q}}} - \frac{\partial L}{\partial \mathbf{q}} = \tilde{\mathbf{Q}} + A^T\lambda \tag{2.1}$$

$$A\dot{\mathbf{q}} = 0 \tag{2.2}$$

where the state vector $\mathbf{q}$ is

$$\mathbf{q} = \begin{bmatrix} x & y & \psi & \theta_1 & \theta_2 & \theta_3 \end{bmatrix}^T \tag{2.3}$$

Because we consider planar mase motions, the potential energy of the system is constant and equal to zero. Therefore $L = T$ and Eqn. (2.1) becomes

$$\frac{d}{dt}\frac{\partial T}{\partial \dot{\mathbf{q}}} - \frac{\partial T}{\partial \mathbf{q}} = \tilde{\mathbf{Q}} + A^T\lambda \tag{2.4}$$

The constraint matrix $A$ is constructed by imposing the nonholonomic no-sideslip constraint on the caster wheels. We can obtain the generalized forces $\tilde{\mathbf{Q}}$ by evaluating the work rate and the total kinetic energy $T$ can be computed using the translational and rotational motion of the system.

The system geometry is shown in Fig. 3. When developing the dynamic model, three reference frames were used. The fixed inertial frame is denoted by the $\hat{n}_1$ and $\hat{n}_2$ axes, the main body frame by $\hat{b}_1$ and $\hat{b}_2$, and the caster frame by $\hat{c}_1$ and $\hat{c}_2$. HOMER's planar motion is defined by translational movement in $x$ and $y$ and rotational movement designated by $\psi$. The geometry of the main body has an effective radius $R$ and the angle $\phi_i$ represents the angle between the body axis $\hat{b}_1$ and the point $P_i$. Each caster angle, $\theta_i$, denotes the rotation between each caster frame and the body

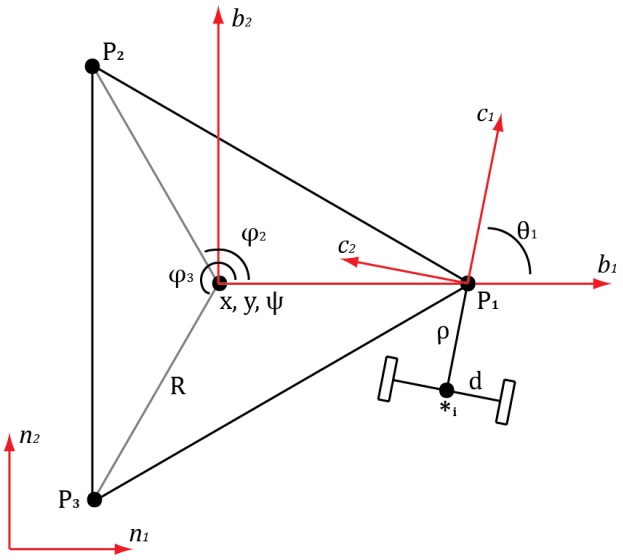


Fig. 3. Geometry of HOMER's Base

frame. Lengths $\rho$ and $d$ define the geometry of each caster. The main body's mass and moment of inertia about its mass center is defined by $m_1$ and $I$, respectively. Similarly, the masses and moments of inertia of each caster about its pivot point are equal and are denoted by $m_2$ and $J$, respectively.

First, the inertial position of point $\star_i$ is specified in the caster frame

$$ {}^{N}\mathbf{p}_{\star_i} = \mathbf{CB} \begin{bmatrix} x \\ y \\ 0 \end{bmatrix} + \mathbf{C} \begin{bmatrix} R\cos\phi_i \\ R\sin\phi_i \\ 0 \end{bmatrix} + \begin{bmatrix} -\rho \\ 0 \\ 0 \end{bmatrix} \tag{2.5} $$

where the rotation matrices $\mathbf{B}$ and $\mathbf{C}$ are defined as

$$ \mathbf{B} = \begin{bmatrix} \cos(\psi) & \sin(\psi) & 0 \\ -\sin(\psi) & \cos(\psi) & 0 \\ 0 & 0 & 1 \end{bmatrix}, \quad \mathbf{C} = \begin{bmatrix} \cos(\theta_i) & \sin(\theta_i) & 0 \\ -\sin(\theta_i) & \cos(\theta_i) & 0 \\ 0 & 0 & 1 \end{bmatrix} \tag{2.6} $$

The transport theorem is defined as [10]

$$^{N}\dot{\mathbf{r}} = {}^{A}\dot{\mathbf{r}} + \omega_{A/N} \times {}^{A}\mathbf{r} \tag{2.7}$$

Using this theorem, the caster frame components of the inertial velocity of point $\star_i$ become

$$^{N}\mathbf{v}_{\star_i} = \mathbf{CB}\begin{bmatrix}\dot{x}\\ \dot{y}\\ 0\end{bmatrix} + \mathbf{C}\begin{bmatrix}-\dot{\psi}R\sin\phi_i\\ \dot{\psi}R\cos\phi_i\\ 0\end{bmatrix} + \begin{bmatrix}0\\ -\rho(\dot{\psi}+\dot{\theta}_i)\\ 0\end{bmatrix} \tag{2.8}$$

The no-sideslip constraint dictates that the inertial velocity in the 2-direction of the caster frame must equal zero. Mathematically,

$$^{N}\mathbf{v}_{\star_i} \cdot \hat{\mathbf{c}}_2 = 0 \tag{2.9}$$

Imposing this constraint on each of the three casters produces three scalar equations which can be rewritten as Eqn. (2.2)

$$\mathbf{A}\dot{\mathbf{q}} = \begin{bmatrix}-\sin(\psi+\theta_1) & \cos(\psi+\theta_1) & R\cos(\theta_1-\phi_1)-\rho & -\rho & 0 & 0\\ -\sin(\psi+\theta_2) & \cos(\psi+\theta_2) & R\cos(\theta_2-\phi_2)-\rho & 0 & -\rho & 0\\ -\sin(\psi+\theta_3) & \cos(\psi+\theta_3) & R\cos(\theta_3-\phi_3)-\rho & 0 & 0 & -\rho\end{bmatrix}\begin{bmatrix}\dot{x}\\ \dot{y}\\ \dot{\psi}\\ \dot{\theta}_1\\ \dot{\theta}_2\\ \dot{\theta}_3\end{bmatrix} = 0 \tag{2.10}$$

The no-slip rotation of the two caster wheels completely dictate the motion of each caster, and therefore its pivot point motion.

## A. Generalized Forces

The system is made up of the rigid main body, the three casters, and the six wheels. The generalized forces vector $\tilde{\mathbf{Q}}$ can be constructed by evaluating the work rate of the system and then extracting the coefficients of the velocity terms defined by Eqn. (2.3). When considering the main body and caster interaction, forces do exist. However, the generalized forces vector $\tilde{\mathbf{Q}}$ represents the sum of forces for the entire system. Therefore, we can ignore any forces on the main body exerted from the caster because opposite and equal forces exist when considering each caster.

The work rate expression for the system is

$$\dot{W}_i = \tau_{Ri} \cdot \omega_{Ri} + \tau_{Li} \cdot \omega_{Li} + \mathbf{F}_{fRi} \cdot \mathbf{v}_{RCi} + \mathbf{F}_{fLi} \cdot \mathbf{v}_{LCi} \tag{2.11}$$

where $\tau_{Ri}$ and $\tau_{Li}$ are the torques acting on each wheel, $\omega_{Ri}$ and $\omega_{Li}$ represent the angular velocities of the wheels, $\mathbf{F}_{fRi}$ and $\mathbf{F}_{fLi}$ are the frictional forces, and the velocities $\mathbf{v}_{RCi}$ and $\mathbf{v}_{LCi}$ represent the velocity of the point on the wheel that is in contact with the ground. Because the wheels roll without slip, the inertial velocity on each wheel at the point of contact is zero. Therefore, Eqn. (2.11) becomes

$$\dot{W}_i = \tau_{Ri} \cdot \omega_{Ri} + \tau_{Li} \cdot \omega_{Li} \tag{2.12}$$

The angular velocities are related to the translational velocity of the mass center of each wheel.

$$\omega_{Ri} = \frac{\mathbf{v}_{Ri}}{r}, \qquad \omega_{Li} = \frac{\mathbf{v}_{Li}}{r} \tag{2.13}$$

where $\mathbf{v}_{Ri}$ and $\mathbf{v}_{Li}$ are the inertial velocities of the wheel mass centers and $r$ is the wheel radius. Additionally, each torque is related to an effective force applied to the wheel and its radius $r$.

$$\mathbf{F}_{Ri} = \frac{\tau_{Ri}}{r}, \qquad \mathbf{F}_{Li} = \frac{\tau_{Li}}{r} \tag{2.14}$$

Thus, the work rate expression can be written as

$$\dot{W}_i = \mathbf{F}_{Ri} \cdot \mathbf{v}_{Ri} + \mathbf{F}_{Li} \cdot \mathbf{v}_{Li} \tag{2.15}$$

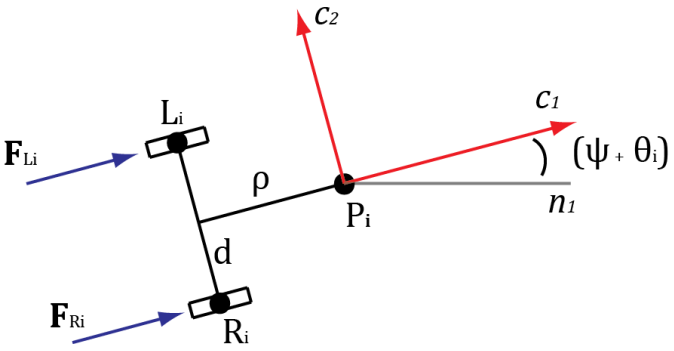


Fig. 4. Geometry of HOMER's Casters

The inertial velocities at points $R_i$ and $L_i$, as seen in Fig. 4, can be defined as

$${}^N\mathbf{v}_{Ri} = {}^N\mathbf{v}_{Pi} + \begin{bmatrix} 0 \\ 0 \\ (\dot{\psi} + \dot{\theta}_i) \end{bmatrix} \times \begin{bmatrix} -\rho \\ -d \\ 0 \end{bmatrix} \tag{2.16}$$

$${}^N\mathbf{v}_{Li} = {}^N\mathbf{v}_{Pi} + \begin{bmatrix} 0 \\ 0 \\ (\dot{\psi} + \dot{\theta}_i) \end{bmatrix} \times \begin{bmatrix} -\rho \\ d \\ 0 \end{bmatrix} \tag{2.17}$$

where $\mathbf{v}_{Pi}$ is defined as

$${}^N\mathbf{v}_{Pi} = \mathbf{CB} \begin{bmatrix} \dot{x} \\ \dot{y} \\ 0 \end{bmatrix} + \mathbf{C} \begin{bmatrix} -\dot{\psi} R \sin\phi_i \\ \dot{\psi} R \cos\phi_i \\ 0 \end{bmatrix} \tag{2.18}$$

If we define the exerted forces as

$$ {}^{C}\mathbf{F}_{Ri} = \begin{bmatrix} F_{Ri} \\ 0 \\ 0 \end{bmatrix}, \quad {}^{C}\mathbf{F}_{Li} = \begin{bmatrix} F_{Li} \\ 0 \\ 0 \end{bmatrix} \tag{2.19} $$

Then, for each of the three casters, the work rate becomes

$$ \begin{aligned} \dot{W}_i =& [(F_{Ri} + F_{Li})\cos(\psi + \theta_i)]\dot{x} + [(F_{Ri} + F_{Li})\sin(\psi + \theta_i)]\dot{y} + \\ &+ [(F_{Ri} + F_{Li})R\sin(\theta_i - \phi_i) + (F_{Ri} - F_{Li})d]\dot{\psi} + [(F_{Ri} - F_{Li})d]\dot{\theta}_i \end{aligned} \tag{2.20} $$

By summing the work rate of the casters, it is possible to construct $\tilde{\mathbf{Q}}$ where each element in the vector is the coefficient of the respective velocity term.

$$ \tilde{\mathbf{Q}} = \begin{bmatrix} Q_x & Q_y & Q_\psi & Q_{\theta_1} & Q_{\theta_2} & Q_{\theta_3} \end{bmatrix}^T \tag{2.21} $$

For simulation purposes, $\tilde{\mathbf{Q}}$ is redefined

$$ \tilde{\mathbf{Q}} = D\mathbf{u} \tag{2.22} $$

where $D$ is the $6 \times 6$ direct transmission matrix and $\mathbf{u}$ is the input vector

$$ \mathbf{u} = \begin{bmatrix} F_{R1} & F_{R2} & F_{R3} & F_{L1} & F_{L2} & F_{L3} \end{bmatrix}^T \tag{2.23} $$

B. Kinetic Energy and the Mass Matrix

There are several ways to calculate the total kinetic energy of this multi-body system. Here, the most common approach is taken where the translational and rotational energy of each body is summed. The total kinetic energy of HOMER's base is defined as

$$ T = T_B + T_{C1} + T_{C2} + T_{C3} \tag{2.24} $$

where the kinetic energy of the main body, $T_B$, is simply

$$T_B = \frac{1}{2}m_1(\dot{x}^2 + \dot{y}^2) + \frac{1}{2}I\dot{\psi}^2 \tag{2.25}$$

Based on the geometry of the robot, it is assumed that each caster's center of mass resides at the pivot point $P_i$. Therefore the kinetic energy of each caster, $T_{Ci}$, becomes

$$T_{Ci} = \frac{1}{2}m_2(\mathbf{v}_{Pi} \cdot \mathbf{v}_{Pi}) + \frac{1}{2}J(\dot{\psi} + \dot{\theta}_i)^2 \tag{2.26}$$

where $\mathbf{v}_{Pi}$ has been previously defined in Eqn. (2.18). The dot product $\mathbf{v}_{Pi} \cdot \mathbf{v}_{Pi}$ can be expanded

$$\begin{aligned}\mathbf{v}_{Pi} \cdot \mathbf{v}_{Pi} =& \dot{x}^2 + \dot{y}^2 + \dot{\psi}^2R^2 + \\ &+ 2\dot{x}\dot{\psi}R\cos(\psi + \theta_i)\sin(\theta_i - \phi_i) - 2\dot{x}\dot{\psi}R\sin(\psi + \theta_i)\cos(\theta_i - \phi_i) + \\ &+ 2\dot{y}\dot{\psi}R\sin(\psi + \theta_i)\sin(\theta_i - \phi_i) + 2\dot{y}\dot{\psi}R\cos(\psi + \theta_i)\cos(\theta_i - \phi_i)\end{aligned} \tag{2.27}$$

Equation (2.27) can be reduced using trigonometric angle sum and difference identities.

$$\mathbf{v}_{Pi} \cdot \mathbf{v}_{Pi} = \dot{x}^2 + \dot{y}^2 + \dot{\psi}^2R^2 - 2\dot{x}\dot{\psi}R\sin(\psi + \phi_i) + 2\dot{y}\dot{\psi}R\cos(\psi + \phi_i) \tag{2.28}$$

The total kinetic energy, $T$, becomes

$$\begin{aligned}T =& \frac{1}{2}m_1(\dot{x}^2 + \dot{y}^2) + \frac{1}{2}I\dot{\psi}^2 + \frac{1}{2}J(3\dot{\psi}^2 + 2\dot{\psi}\dot{\theta}_1 + 2\dot{\psi}\dot{\theta}_2 + 2\dot{\psi}\dot{\theta}_3 + \dot{\theta}_1^2) + \dot{\theta}_2^2) + \dot{\theta}_3^2) + \\ &+ \frac{1}{2}m_2\left[\dot{x}^2 + \dot{y}^2 + \dot{\psi}^2R^2 - 2\dot{x}\dot{\psi}R\sin(\psi + \phi_1) + 2\dot{y}\dot{\psi}R\cos(\psi + \phi_1)\right] + \\ &+ \frac{1}{2}m_2\left[\dot{x}^2 + \dot{y}^2 + \dot{\psi}^2R^2 - 2\dot{x}\dot{\psi}R\sin(\psi + \phi_2) + 2\dot{y}\dot{\psi}R\cos(\psi + \phi_2)\right] + \\ &+ \frac{1}{2}m_2\left[\dot{x}^2 + \dot{y}^2 + \dot{\psi}^2R^2 - 2\dot{x}\dot{\psi}R\sin(\psi + \phi_3) + 2\dot{y}\dot{\psi}R\cos(\psi + \phi_3)\right]\end{aligned} \tag{2.29}$$

To obtain the mass matrix, $M$, the total kinetic energy is rewritten as

$$T = \frac{1}{2}\dot{\mathbf{q}}^T M \dot{\mathbf{q}} \tag{2.30}$$

The mass matrix for HOMER's base is defined as

$$M = \begin{bmatrix} m_1 + 3m_2 & 0 & \alpha & 0 & 0 & 0 \\ 0 & m_1 + 3m_2 & \beta & 0 & 0 & 0 \\ \alpha & \beta & I + 3J + 3m_2R^2 & J & J & J \\ 0 & 0 & J & J & 0 & 0 \\ 0 & 0 & J & 0 & J & 0 \\ 0 & 0 & J & 0 & 0 & J \end{bmatrix} \tag{2.31}$$

where

$$\alpha = -m_2 R \left(\sin\left(\psi + \phi_1\right) + \sin\left(\psi + \phi_2\right) + \sin\left(\psi + \phi_3\right)\right) \tag{2.32}$$

$$\beta = m_2 R \left(\cos\left(\psi + \phi_1\right) + \cos\left(\psi + \phi_2\right) + \cos\left(\psi + \phi_3\right)\right) \tag{2.33}$$

The mass matrix is used to write the Lagrangian equations of motion into a more usable form and later, will be partitioned to form the PD controller.

## C. Lagrangian Multiplier

The Lagrangian multiplier vector $\lambda$ must be computed for computer-based simulation and hardware implementation. Using the newly defined mass matrix, Eqn. (2.4) can be rewritten as

$$M\ddot{\mathbf{q}} + \dot{M}\dot{\mathbf{q}} - \mathbf{G} = A^T\lambda + \tilde{\mathbf{Q}} \tag{2.34}$$

where

$$\mathbf{G} = \frac{\partial T}{\partial \mathbf{q}} \tag{2.35}$$

$$M\ddot{\mathbf{q}} + \dot{M}\dot{\mathbf{q}} = \frac{d}{dt}\frac{\partial T}{\partial \dot{\mathbf{q}}} \tag{2.36}$$

By pre-multiplying Eqn. (2.34) components by $AM^{-1}$ and rearranging

$$AM^{-1}A^T\lambda = A\ddot{\mathbf{q}} + AM^{-1}\dot{M}\dot{\mathbf{q}} - AM^{-1}\mathbf{G} - AM^{-1}\tilde{\mathbf{Q}} \tag{2.37}$$

The system of Pfaffian constraints from Eqn. (2.2) can be manipulated by taking the derivative such that

$$A\ddot{\mathbf{q}} + \dot{A}\dot{\mathbf{q}} = 0 \tag{2.38}$$

And, consequently, the Lagrangian vector $\lambda$ can be written as

$$\lambda = (AM^{-1}A^T)^{-1}(-\dot{A}\dot{\mathbf{q}} + AM^{-1}\dot{M}\dot{\mathbf{q}} - AM^{-1}\mathbf{G} - AM^{-1}\tilde{\mathbf{Q}}) \tag{2.39}$$

## D. Motor Model

To ensure an accurate simulation of the hardware, an appropriate motor model is needed. The motor model converts the specified forces in Eqn. (2.23) to voltages applied to each motor. To do this, the inertial velocity of the wheel center is needed. These velocities were calculated earlier in Eqn. (2.16) and Eqn. (2.17) for each caster. The radius of each wheel is used to calculate the angular velocity of the wheel as

$$\omega_w = \frac{v}{r} \tag{2.40}$$

Each motor is equiped with a 7:1 gearbox. Therefore the angular velocity of each driveshaft at the motor is

$$\omega_m = 7\omega_w \tag{2.41}$$

The required torque of the motor is computed using the required force, wheel radius, and gearbox ratio.

$$\tau_m = \frac{7}{Fr} \tag{2.42}$$

These angular velocity and torque values at the motor are used to calculate the

required voltage, $V$, for each motor; all use the following idealized linear model:

$$V = K_v \omega_m + \frac{R_c \tau_m}{K_t} \tag{2.43}$$

where $K_v = 9.08$ V/kRPM, $K_t = 12.28$ oz-in/Amp, and $R_c = 0.74$ Ohms are specified motor constants. This particular motor model uses a steady-state assumption in which an applied current is constant. Realistically, an applied current would experience a transient and the motor model would contain an additional current state to take this transient into account. The steady-state assumption was implemented to limit the amount of variables that required numerical solving in the computer-based simulations.

# CHAPTER III

## CONTROL

HOMER's base provides an interesting control problem because there are six system configuration coordinates but it is only necessary to control three of those coordinates. It is not required to control the caster angles, but they still need to be measured because they appear in the kinematics. The casters are only required to behave such that $x$, $y$, and $\psi$ sufficiently track their respective reference trajectories. This property allows for partitioning of the dynamics to simplify the control problem and develop a Lyapunov function that drives the error in $x$, $y$, and $\psi$ to zero.

Before partitioning the dynamics, the equations of motion need to be rearrange in such a way that the control vector $\mathbf{u}$ can be isolated. Using the variables defined in Ch. II, Eqn. (2.4) becomes

$$M\ddot{\mathbf{q}} + \dot{M}\dot{\mathbf{q}} - \mathbf{G} - A^T\lambda = D\mathbf{u} \tag{3.1}$$

However, $\lambda$ contains $\tilde{\mathbf{Q}}$ as seen in Eqn. (2.39), which is equal to $D\mathbf{u}$. Therefore, $D\mathbf{u}$ must be extracted from the left hand side of the equation. Substituting Eqn. (2.39) into Eqn. (3.1) gives

$$M\ddot{\mathbf{q}}+\dot{M}\dot{\mathbf{q}}-\mathbf{G}-A^T\left[(AM^{-1}A^T)^{-1}(-\dot{A}\dot{\mathbf{q}} + AM^{-1}\dot{M}\dot{\mathbf{q}} - AM^{-1}\mathbf{G} - AM^{-1}D\mathbf{u})\right] = D\mathbf{u} \tag{3.2}$$

A new vector, $\mathbf{S}$, is defined as

$$\mathbf{S} = (AM^{-1}A^T)^{-1}(-\dot{A}\dot{\mathbf{q}} + AM^{-1}\dot{M}\dot{\mathbf{q}} - AM^{-1}\mathbf{G}) \tag{3.3}$$

Then, Eqn. (3.2) becomes

$$M\ddot{\mathbf{q}} + \dot{M}\dot{\mathbf{q}} - \mathbf{G} - A^T\mathbf{S} + A^T(AM^{-1}A^T)^{-1}(AM^{-1}D\mathbf{u}) = D\mathbf{u} \tag{3.4}$$

This can be rewritten as

$$M\ddot{\mathbf{q}} + \dot{M}\dot{\mathbf{q}} - \mathbf{G} - A^T\mathbf{S} = \left[D - A^T(AM^{-1}A^T)^{-1}(AM^{-1}D)\right]\mathbf{u} \tag{3.5}$$

In an effort to ease the partitioning process, two additional variables, $f$ and $H$, are introduced.

$$\mathbf{f} = \dot{M}\dot{\mathbf{q}} - \mathbf{G} - A^T\mathbf{S} \tag{3.6}$$

$$H = D - A^T(AM^{-1}A^T)^{-1}(AM^{-1}D) \tag{3.7}$$

These new variables give way to a simplified version of Eqn. (3.1)

$$M\ddot{\mathbf{q}} + \mathbf{f} = H\mathbf{u} \tag{3.8}$$

## A. Partitioned Dynamics

One goal is to determine a control that minimizes the error in the coordinates $x$, $y$, and $\psi$, which represent a portion of the generalized configuration coordinate vector $\mathbf{q}$. These coordinates describe the planar motion of the base. The equations that govern these coordinates can be isolated in a straightforward way by partitioning Eqn. (3.8).

$$\begin{bmatrix} M_{11} & M_{12} \\ M_{21} & M_{22} \end{bmatrix} \begin{bmatrix} \ddot{\mathbf{q}}_1 \\ \ddot{\mathbf{q}}_2 \end{bmatrix} + \begin{bmatrix} \mathbf{f}_1 \\ \mathbf{f}_2 \end{bmatrix} = \begin{bmatrix} H_1 \\ H_2 \end{bmatrix} \mathbf{u} \tag{3.9}$$

where

$$\mathbf{q}_1 = \begin{bmatrix} x & y & \psi \end{bmatrix}^T, \quad \mathbf{q}_2 = \begin{bmatrix} \theta_1 & \theta_2 & \theta_3 \end{bmatrix}^T \tag{3.10}$$

It is possible to separate Eqn. (3.9) into two partitioned equations to form

$$M_{11}\ddot{\mathbf{q}}_1 + M_{12}\ddot{\mathbf{q}}_2 + \mathbf{f}_1 = H_1\mathbf{u} \tag{3.11}$$

$$M_{21}\ddot{\mathbf{q}}_1 + M_{22}\ddot{\mathbf{q}}_2 + \mathbf{f}_2 = H_2\mathbf{u} \tag{3.12}$$

Because we're only interested in controlling $\mathbf{q}_1$, we solve Eqn. (3.12) for $\ddot{\mathbf{q}}_2$

$$\ddot{\mathbf{q}}_2 = M_{22}^{-1}[H_2\mathbf{u} - \mathbf{f}_2 - M_{21}\ddot{\mathbf{q}}_1] \tag{3.13}$$

which can be substituted into Eqn. (3.11) to form

$$M_{11}\ddot{\mathbf{q}}_1 + M_{12}M_{22}^{-1}[H_2\mathbf{u} - \mathbf{f}_2 - M_{21}\ddot{\mathbf{q}}_1] + \mathbf{f}_1 = H_1\mathbf{u} \tag{3.14}$$

and simplified to

$$\ddot{\mathbf{q}}_1 = \tilde{M}^{-1}[\tilde{H}\mathbf{u} - \tilde{\mathbf{f}}] \tag{3.15}$$

where

$$\tilde{M} = M_{11} - M_{12}M_{22}^{-1}M_{21} \tag{3.16}$$

$$\tilde{\mathbf{f}} = \mathbf{f}_1 - M_{12}M_{22}^{-1}\mathbf{f}_2 \tag{3.17}$$

$$\tilde{H} = H_1 - M_{12}M_{22}^{-1}H_2 \tag{3.18}$$

This method of partitioned dynamics allows control of the 3-DOF motion, $\mathbf{q}_1$, regardless of the caster angles, $\mathbf{q}_2$. It is necessary, however, to measure the caster angles because they are found in Eqn. (3.15). These angles are measured with encoders that feed into the onboard filter, and hence, into the controller. The associated measured errors are an issue that must be evaluated; in the present case, these small errors do not significantly degrade the performance.

## B. Lyapunov Stability

A typical, quadratic Lyapunov function is selected which utilizes gains $K_1$ and $K_2$

$$V = \frac{1}{2}\dot{\mathbf{e}}^T K_1 \dot{\mathbf{e}} + \frac{1}{2}\mathbf{e}^T K_2 \mathbf{e} \tag{3.19}$$

$$\dot{V} = \dot{\mathbf{e}}^T K_1 \ddot{\mathbf{e}} + \dot{\mathbf{e}}^T K_2 \mathbf{e} \tag{3.20}$$

To drive the tracking error of $\mathbf{q}_1$ to zero, $(\ddot{\mathbf{q}}_1 - \ddot{\mathbf{q}}_r)$ is substituted for $\ddot{\mathbf{e}}$

$$\dot{V} = \dot{\mathbf{e}}^T[K_1(\ddot{\mathbf{q}}_1 - \ddot{\mathbf{q}}_r) + K_2\mathbf{e}] \tag{3.21}$$

For tracking stability, $\dot{V}$ should be negative semi-definite. This yields the solution

$$K_1(\ddot{\mathbf{q}}_1 - \ddot{\mathbf{q}}_r) + K_2\mathbf{e} = -\dot{\mathbf{e}} \tag{3.22}$$

By substituting Eqn. (3.15) in, we have

$$K_1\left[\tilde{M}^{-1}(\tilde{H}\mathbf{u} - \tilde{\mathbf{f}}) - \ddot{\mathbf{q}}_r\right] + K_2\mathbf{e} = -\dot{\mathbf{e}} \tag{3.23}$$

Which can then be rewritten as

$$\tilde{M}^{-1}\tilde{H}\mathbf{u} = \ddot{\mathbf{q}}_r + \tilde{M}^{-1}\tilde{\mathbf{f}} - K_1^{-1}\dot{\mathbf{e}} - K_1^{-1}K_2\mathbf{e} \tag{3.24}$$

$K_1$ and $K_2$ are arbitrary, so they can be redefined to simplify Eqn. (3.24).

$$\tilde{M}^{-1}\tilde{H}\mathbf{u} = \ddot{\mathbf{q}}_r + \tilde{M}^{-1}\tilde{\mathbf{f}} - K_2\dot{\mathbf{e}} - K_1\mathbf{e} \tag{3.25}$$

The control vector $\mathbf{u}$ is dimensioned $6 \times 1$, thus a rank 3 pseudoinverse is used to compute the minimum norm force required to stably track the desired motion. Mathematically, this transforms Eqn. (3.25) into

$$\mathbf{u} = \left[\tilde{M}^{-1}\tilde{H}\right]^T\left[\tilde{M}^{-1}\tilde{H}\tilde{H}^T\tilde{M}^{-T}\right]^{-1}\left[\ddot{\mathbf{q}}_r + \tilde{M}^{-1}\tilde{\mathbf{f}} - K_1\mathbf{e} - K_2\dot{\mathbf{e}}\right] \tag{3.26}$$

Of course, this is only valid if the inverse of $\tilde{M}^{-1}\tilde{H}\tilde{H}^T\tilde{M}^{-T}$ exists. This form of control is commonly referred to as proportional-derivative or PD control because the position error and its derivative are fed into the controller.

## C. Voltage Limiter

The required torque each motor can exert is limited by the voltage supply of the batteries. To ensure only feasible torques are commanded during computer-based simulation, a voltage limiter is integrated into the motor model. After the controller computes the required forces to move the base as requested, the forces are input into the motor model described in Eqn. (2.43). As a result, voltage commands are produced. These voltages are then limited at +/-24 V. The limited voltages are then run back through the motor model to output the actual forces that the motors would be capable of exerting on the ground. The closed loop performance evaluation discussed in Ch. VII includes consideration of this control saturation effect. It is possible for this control saturation effect to have negative influences when implemented on the hardware. Fortunately, extensive experimental testing has proved that these voltage limits are never approached during hardware simulations.

# CHAPTER IV

# ROBUSTNESS ANALYSIS

## A. Considerations

Before implementing the controller on HOMER, an in-depth robustness analysis was conducted to see how possible errors may effect the system performance. There are several factors to consider when working with hardware including errors in the mass and moment of inertia estimates, measurement noise from the sensing systems, and latencies found within the sensing systems, communication links, and the onboard controller. Several combinations of these errors were introduced at different magnitudes for the same reference maneuver. The reference maneuver selected was comprised of a circle with a 1.5 m radius and a heading varied to remain pointing at the center of the circle, which exemplifies the characteristics of a typical lunar orbit. The maneuver velocities and accelerations were specified based on the maximum velocity and acceleration the hardware is capable of. The maximum acceleration was applied until the maximum velocity was reached. A deceleration of the same magnitude was then applied towards the end of the reference maneuver to bring the system to rest at the starting point.

### 1. Mass and Moment of Inertia Errors

The mass of HOMER was estimated using computer aided drawing (CAD) models of the major structural elements, but did not include items such as the electronics. It was assumed that the center of mass was located at the geometric center of the body. The moments of inertia of HOMER were estimated by assuming the main body was a solid cylinder of the appropriate mass and radius while the casters were assumed

to be solid bricks. Therefore, the true mass and moments of inertia were varied by a percent of the assumed nominal value over the range [80%,120%] in 10% increments during the robustness analysis. The estimated model mass and moment of inertia values used in the controller remained fixed at the nominal values.

### 2. Measurement Noise

A zero-jerk Kalman filter is built into the sensing system framework to minimize noise on the measurements fed back to the controller, but some noise in the position and velocity measurements must still be accounted for. The nominal $\sigma$ noise characteristics are shown in Table II. For the robustness analysis, simulations were run using zero noise error, the nominal values, and twice the nominal values.

Table II. Nominal Noise Characteristics

| Coordinate | $\sigma$ Value | Units |
|---|---|---|
| $x, y$ | 0.3000 | mm |
| $\psi$ | 0.0167 | deg |
| $\dot{x}, \dot{y}$ | 0.1500 | mm/s |
| $\dot{\psi}$ | 0.0083 | deg/s |

### 3. Latency

Though the controller has not been designed with latency in mind, the hardware implementation will certainly involve some level of latency. To study its impact, a latency of 0.24 s (six time steps for the 25 Hz computer-based controller) was

implemented during the robustness analysis. Preliminary testing of the overall system latency indicates this is a reasonable estimate of the latency that will be encountered on the actual hardware.

## 4. Baseline Gain Analysis

Before running the robustness simulations, appropriate gain values were needed for $K_1$ and $K_2$. To determine these gains, a baseline simulation was specified for both latency intervals. Measurement noise was set to zero along with the mass and moment of inertia errors. The gains were tuned using a grid search method to minimize the position and orientation errors for these three specific cases. These same gain values and latency combinations were used for the robustness analysis simulations with variations in noise and the mass and moment of inertia errors. The gain and latency pairs are summarized in Table III.

Table III. Sensitivity Analysis Gains

| Gain | Zero Latency | 0.24 s Latency |
|---|---|---|
| $K_P$ | 10 | 5 |
| $K_D$ | 10 | 4.5 |

The gains $K_P$ and $K_D$ make up the elements of the gain matrices $K_1$ and $K_2$ found in Eqn. (3.25). These relations are summarized in Eqn. (4.1) where $I_{3\times3}$ represents a $3 \times 3$ identity matrix.

$$K_1 = K_P I_{3\times3}, \quad K_2 = K_D I_{3\times3} \tag{4.1}$$

## B. Results

The reference maneuver was simulated using all combinations of the aforementioned errors with the gains $K_1$ and $K_2$ tweaked for the specific latency error of each simulation. Because the high precision Stewart platform would normally reside on top of HOMER's base, we are interested in tracking position and orientation within one cm and 0.01 rad, respectively. If the tracking errors reside within these bounds, the Stewart platform will be able to compensate and provide a high precision, ground-based hardware simulation.

A Monte Carlo simulation was performed in which 100 runs for each combination of noise, inertia error, and latency were simulated and the results averaged to reduce the variation from the zero-mean Gaussian noise. The maximum tracking error encountered throughout the simulation was recorded to determine if the controller tracked the entire reference trajectory within the target accuracies. Figure 5 shows the errors in position and orientation for the zero latency case, whereas the results with 0.24 s latency are shown in Fig. 6.

As can be seen in Fig. 5, the maximum errors never exceed the target specifications, even with twice the nominal noise and up to 20% errors in mass and moments of inertia. When latency is introduced, the stability guarantee of the Lyapunov-based PD controller no longer holds. Figure 6 shows that when the true inertias are less than the modeled inertias, the controller overcompensates based on latent measurements and may drive the system unstable. Experimentation reveals that by tuning the gains to the expected latency, the target accuracies can be achieved, regardless of what the true mass and moment of inertia values may be (within reason). More importantly, even with a quarter-second latency, twice the expected noise, and a model that underestimates the system inertia by 20%, HOMER's base tracks the

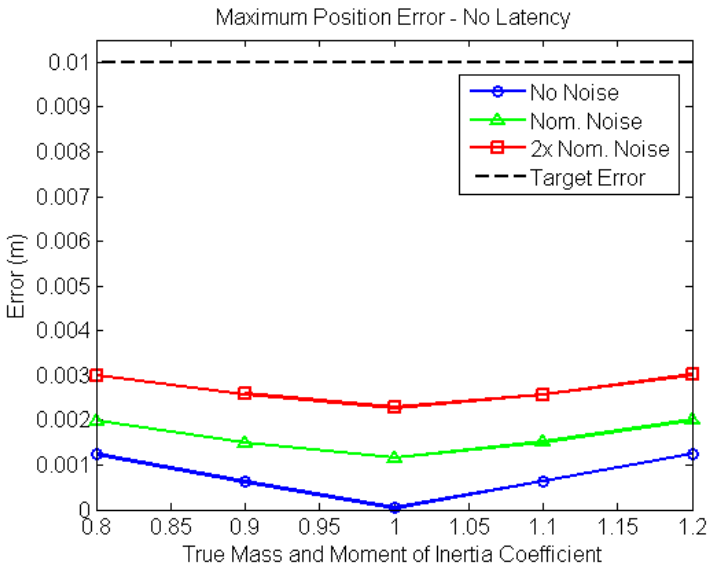


(a) Position errors

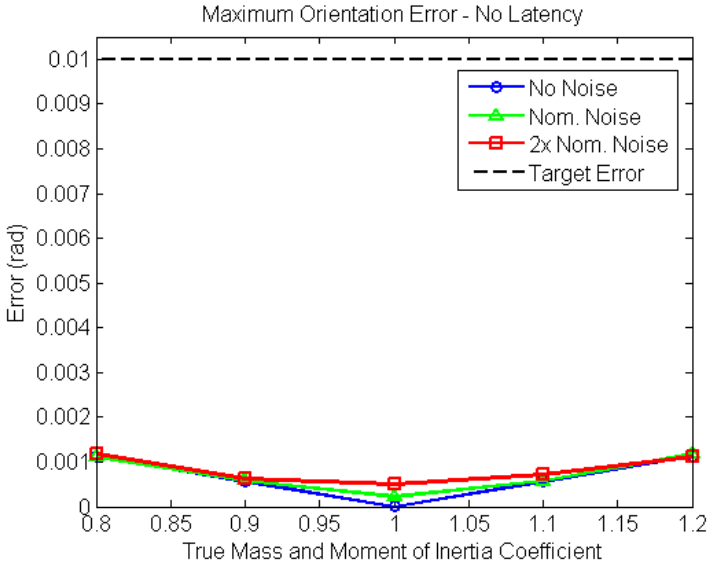


(b) Orientation errors

Fig. 5. Maximum Tracking Error (No Latency)

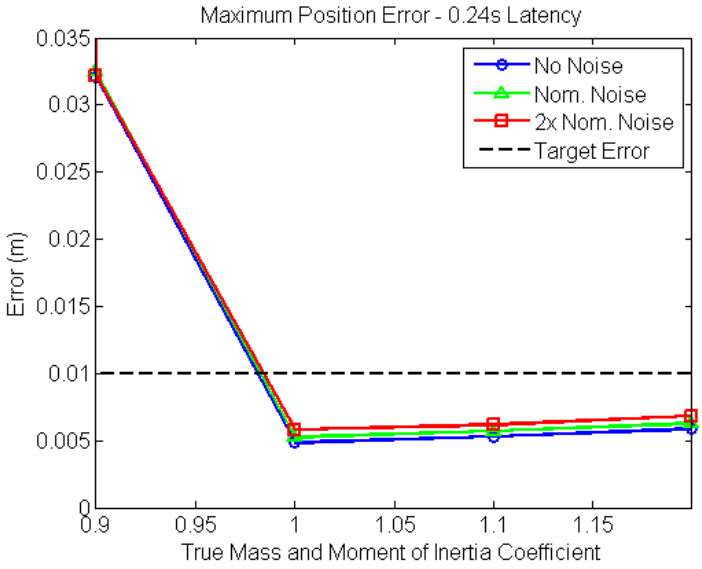


(a) Position errors

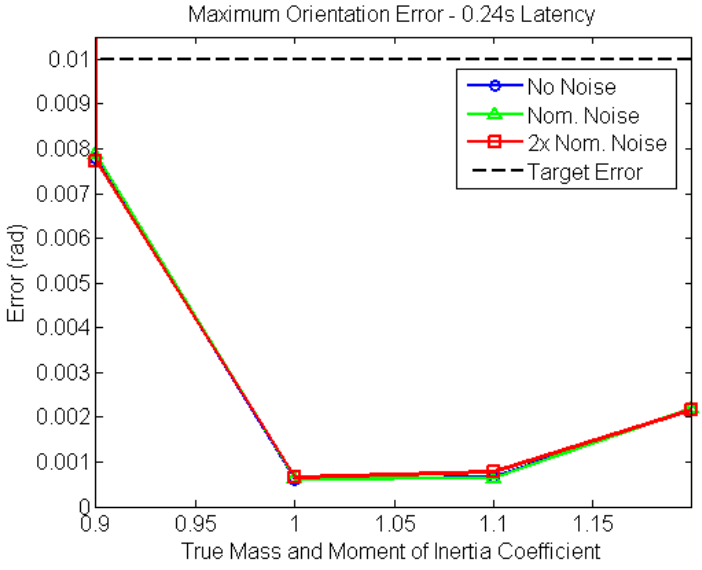


(b) Orientation errors

Fig. 6. Maximum Tracking Error (0.24 s Latency)

reference trajectory within the target tolerances in simulation. Thus, the system is judged to robustly track ideal smooth motions, even with worse than expected model uncertainty, latency, and measurement noise.

# CHAPTER V

## EXPERIMENTATION

Before the feedback controller could be properly implemented on the hardware, several challenges had to be addressed. These challenges distinguish the vast differences between computer-based simulation and real-world validation. The most apparent issue that needed to be dealt with involved feeding the position and velocity measurements from the sensing systems to HOMER's onboard computer. Because the sensing systems only offer position data, it is necessary to compute the velocities based on the sensing system data that is sent to HOMER. Due to variations in measurement times, the external measurements from the sensing systems needed to be synced with the proper onboard measurements of the wheel and caster encoders. By the time the external measurements make it to the onboard computer and velocity is computed, there is inherent latency present between the external measurements that were taken at a previous time and the onboard measurements taken at the current time.

The laboratory sensing system framework compiles the measurements from each of the sensing systems, converts it to a common frame and common time, then broadcasts the data over the laboratory network. Every broadcasted data packet contains the position and orientation of each rigid body defined in the workspace.

HOMER's onboard computer relies on a continuous-discrete extended Kalman filter to process the measurements from the sensing system framework as well as the onboard measurements. The onboard measurements include wheel and caster angular positions through the use of rotary encoders. This onboard filter calculates translational and angular velocities from the broadcasted data then propagates the filter states forward in time based on each measurement's timestamp and the dynamic

model to give the controller a better estimate of what its position and velocity will be when the control is applied.

## A. Tuning

Several gains are present in the control law that act on the translational position and velocity errors and the orientation and angular rate errors. The robustness analysis provided a ballpark range for these gains, which served as a good starting point for the gain tuning. Initially, a linear systems theory approach was taken. Damping coefficients and response frequencies were used to compute suitable gains for a desired performance. This method proved to be semi-effective. Although a theoretical response was obtained, the robot was unable to trap the specified target error. It is possible that the non-linear system paired with latency and noise presented too much deviation from theory. Then, several runs were taken for a combination of these gains and a position or velocity gain was incrementally increased until an envelope of translational gains was studied. After the entire envelope was tested, the combination that produced the least position (and orientation) error and no instances of instability was selected. The final gains selected were $K_P = 28$ and $K_D = 1$. Their relation to the gain matrices $K_1$ and $K_2$ have been previously defined in Eqn. (4.1).

## B. Reference Trajectory Generation

Finally, a realistic reference trajectory that incorporated the characteristics of a proximity operations experiment was needed. A reference trajectory similar to that found in Ch. IV was used. A circle of radius one meter was generated with a heading constantly oriented towards the center. The $x$, $y$, and $\psi$ components of this reference trajectory can be seen in Figures 7, 8, and 9, respectively. In an effort to explore the

entire kinematic workspace, or all physical velocity and acceleration capabilities of HOMER, a Kinematic Workspace Coefficient (KWC) was introduced. The KWC is a value between 0 and 1.0 which represents a percentage of the maximum velocities and accelerations the robot is capable of. For the PD experiments, KWC values of 0.5, 0.75, and 1.0 were used to generate the following trajectories. It should be noted that a KWC of 1.0 was used to generate all reference trajectories up to this point.

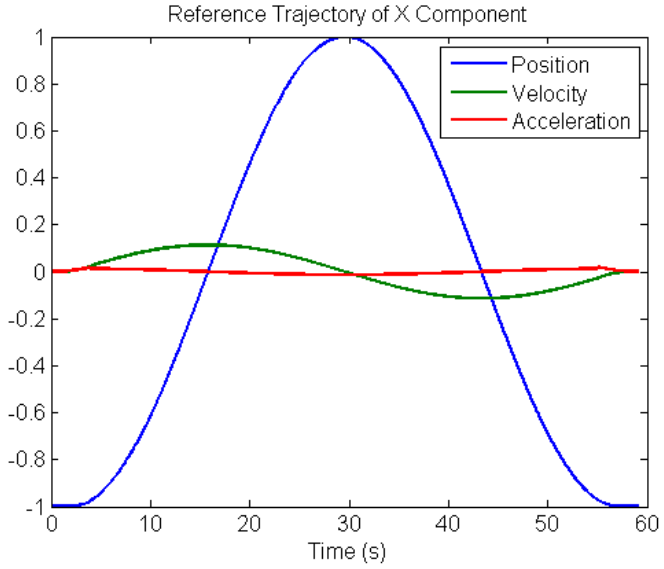


Fig. 7. X-direction Reference Trajectory

## C. PD Results

Each reference trajectory was run ten times at each of the three KWCs for a total of 30 hardware simulations using the feedback PD controller. The experimental results are summarized in Figs. 10 through 13. The mean position error shown in Fig. 10 represents the maximum value of translational error witnessed averaged over ten runs at the specificed KWC. The translational error is defined by the magnitude of

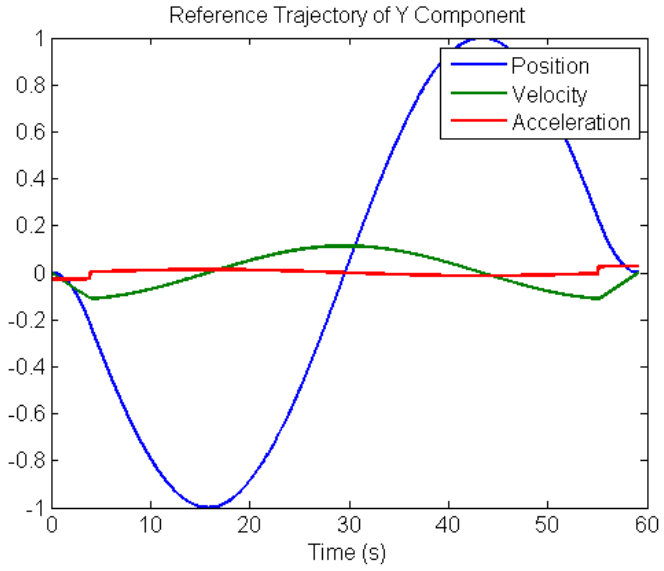


Fig. 8. Y-direction Reference Trajectory

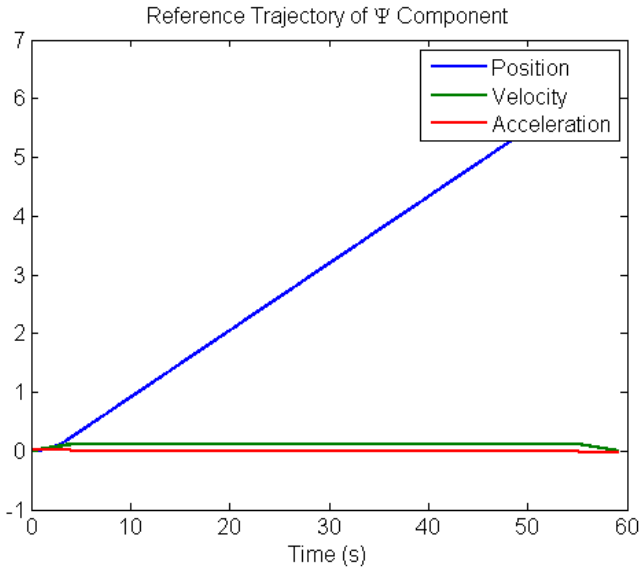


Fig. 9. Rotation ($\Psi$) Reference Trajectory

error measured in the x- and y-directions. Error bars are also shown using using one standard deviation of the maximum errors. The mean velocity errors shown in Fig. 11 were computed similarly.

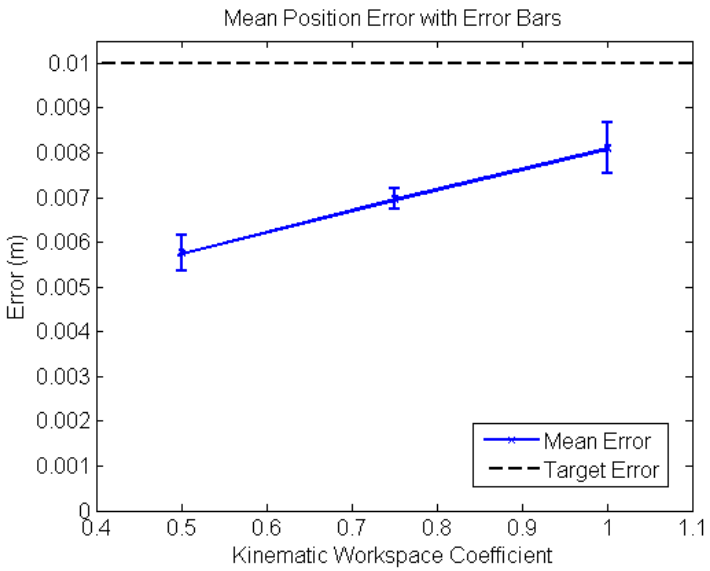


Fig. 10. Mean Maximum PD Position Error

The mean orientation errors measured are shown in Fig. 12. Because HOMER's base has three degrees of freedom, these orientation errors simply represent the magnitude of the error witnessed in the orientation angle $\psi$. The mean angular velocity errors are shown in Fig. 13.

The maximum translational position error values fall within the target value of one cm even at the maximum KWC. The orientation errors, however, do not. Target errors for the velocity level errors were not specified during the design process because it was assumed that at such a high hardware control update rate, the velocity error

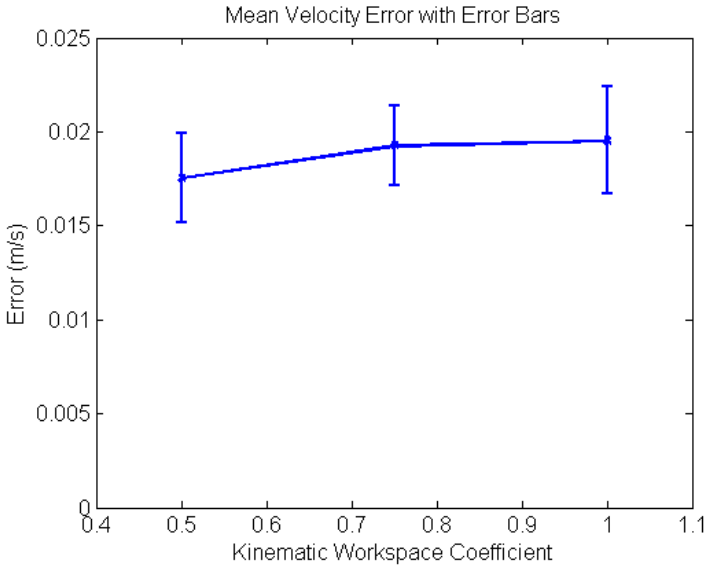


Fig. 11. Mean Maximum PD Velocity Error

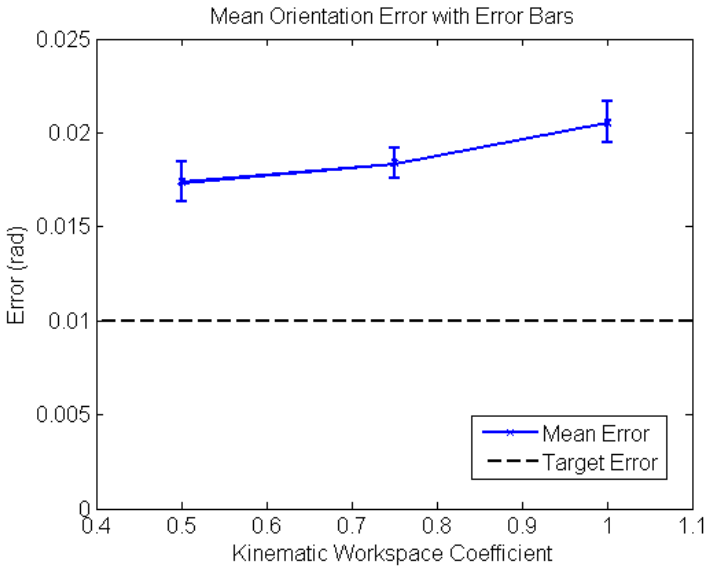


Fig. 12. Mean Maximum PD Orientation Error

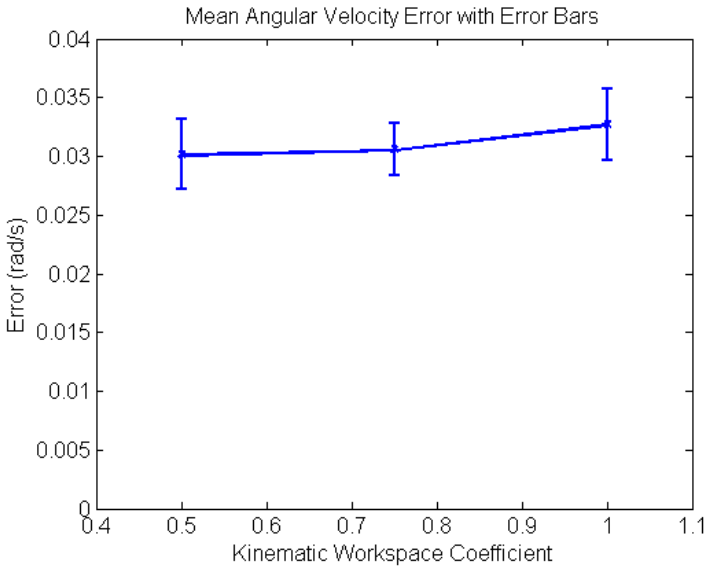


Fig. 13. Mean Maximum PD Angular Velocity Error

would be sufficiently low enough if the position level target errors were trapped. A few trends were noticed during experimentation involving the existence of constant disturbances. The true motion of the robot always seemed to lag behind the reference trajectory. It was also apparent that the slope of the floor played a large role in the tracking accuracy. In an attempt to offset these constant disturbances and potentially trap the target orientation error, an integral term was introduced into the control law.

# CHAPTER VI

## INTRODUCTION OF THE INTEGRAL TERM

The PD results presented in the previous chapter successfully trapped the translational position target error. Unfortunately, the orienatation error did not meet the specified requirements. One difficulty the PD controller is unable to overcome is constant sources of disturbance. Since HOMER weighs approximately 500 lbs, one significant source of disturbance stems from gravity if the floor isn't perfectly flat. Additionally, friction in the motors and gear boxes have not been modeled. The best way to compensate for these modeling errors is to add an integral term to the controller which acts on the accumulation of previous errors. The addition of this term turns the PD controller into a proportional-integral-derivative or PID controller.

### A. Lyapunov Stability

To prove Lyapunov stability of the new PID controller, the error vector is written as

$$\mathbf{x} = \begin{bmatrix} \int \mathbf{e} \\ \mathbf{e} \\ \dot{\mathbf{e}} \end{bmatrix} \tag{6.1}$$

where the error vector $\mathbf{e}$ contains errors in $x$, $y$, and $\psi$. The derivative of $\mathbf{x}$ becomes

$$\dot{\mathbf{x}} = \begin{bmatrix} \mathbf{e} \\ \dot{\mathbf{e}} \\ \ddot{\mathbf{e}} \end{bmatrix} = \begin{bmatrix} 0 & I_{3x3} & 0 \\ 0 & 0 & I_{3x3} \\ -K_2 & -K_1 & -K_3 \end{bmatrix} \mathbf{x} = A\mathbf{x} \tag{6.2}$$

It is assumed $K_1$, $K_2$, and $K_3$ are defined such that $A$ is a Hurwitz matrix. The Lyapunov function is defined as

$$V = \frac{1}{2}\mathbf{x}^T P\mathbf{x} \tag{6.3}$$

The derivative yields

$$\dot{V} = \frac{1}{2}\dot{\mathbf{x}}^T P\mathbf{x} + \frac{1}{2}\mathbf{x}^T P\dot{\mathbf{x}} \tag{6.4}$$

and the substitution of Eqn. (6.2) produces

$$\dot{V} = \frac{1}{2}\mathbf{x}^T A^T P\mathbf{x} + \frac{1}{2}\mathbf{x}^T PA\mathbf{x} \tag{6.5}$$

The Lyapunov Equation states that for any Hurwitz matrix $A$, a matrix $P$ exists such that $Q$ is positive definite as defined by

$$A^T P + PA = -Q \tag{6.6}$$

This definition of $Q$ gives way to

$$\dot{V} = \frac{1}{2}\mathbf{x}^T (-Q)\,\mathbf{x} \tag{6.7}$$

Therefore, stability is achieved and it is possible to extract $\ddot{\mathbf{e}}$ from Eqn. (6.2).

$$\ddot{\mathbf{e}} = -K_1\mathbf{e} - K_2\int \mathbf{e} - K_3\dot{\mathbf{e}} \tag{6.8}$$

Because $\ddot{\mathbf{e}} = \ddot{\mathbf{q}} - \ddot{\mathbf{q}}_r$,

$$\ddot{\mathbf{q}} = \ddot{\mathbf{q}}_r - K_1\mathbf{e} - K_2\int \mathbf{e} - K_3\dot{\mathbf{e}} \tag{6.9}$$

Therefore, the PD controller presented in Eqn. (3.26) becomes a PID controller of the form

$$\mathbf{u} = \left[\tilde{M}^{-1}\tilde{H}\right]^T \left[\tilde{M}^{-1}\tilde{H}\tilde{H}^T\tilde{M}^{-T}\right]^{-1} \left[\ddot{\mathbf{q}}_r + \tilde{M}^{-1}\tilde{\mathbf{f}} - K_1\mathbf{e} - K_2\int \mathbf{e} - K_3\dot{\mathbf{e}}\right] \tag{6.10}$$

B. Tuning

It was necessary to tune the PID gains before comparing experimental results between the two controllers. To simplify this process, translational and rotational gains were tuned independently. Two reference trajectories were generated to decouple the motions. For the translational tuning a straight line motion was used with an initial constant, maximum acceleration to maximum velocity, a hold at maximum velocity, and then a maximum deceleration to rest. The rotational reference trajectory had similar position, velocity, and acceleration profiles, but the motion was a pure spin instead of a straight line. This spin motion started with an initial constant, maximum angular acceleration to maximum angular velocity, followed by a hold at maximum angular velocity, and then a maximum angular deceleration to rest.

A modified version of the Ziegler-Nichols tuning method was employed for the PID tuning [11]. For each type of motion, the integral and derivative gains were set to zero while the proportional gain was increased. This gain was increased until unstable motion was witnessed. Then, the marginally stable value of the proportional gain was designated as the ulimate gain, $K_U$. The error oscillation properties were then examined to determine the period, $P_U$. Using these gain and period values, the Ziegler-Nichols method offers a way to compute effective values for the proportional, integral, and derivative gains denoted by $K_P$, $K_I$, and $K_D$, respectively, as seen in Eqn. (6.11).

$$K_P = 0.6K_U, \quad K_I = \frac{2K_P}{P_U f}, \quad K_D = \frac{K_P P_U}{8} \tag{6.11}$$

Here, $f$ represents the frequency at which the error is being measured. In this particular application, the motors are being commanded and measurements are being logged at 50 Hz. Therefore, $f = 50$ Hz.

This method was used for each of the translational and rotational cases. The

arrangement of these gains with respect to Eqn. (6.10) is shown in Eqn. (6.12)

$$\mathbf{K}_1 = \begin{bmatrix} K_{P_{xy}} & 0 & 0 \\ 0 & K_{P_{xy}} & 0 \\ 0 & 0 & K_{P_\psi} \end{bmatrix}, \quad \mathbf{K}_2 = \begin{bmatrix} K_{I_{xy}} & 0 & 0 \\ 0 & K_{I_{xy}} & 0 \\ 0 & 0 & K_{I_\psi} \end{bmatrix}, \quad \mathbf{K}_3 = \begin{bmatrix} K_{D_{xy}} & 0 & 0 \\ 0 & K_{D_{xy}} & 0 \\ 0 & 0 & K_{D_\psi} \end{bmatrix} \tag{6.12}$$

Table IV. PID Controller Values

| Gain | Value |
|---|---|
| $K_{U_{xy}}$ | 88 |
| $K_{P_{xy}}$ | 53 |
| $K_{I_{xy}}$ | 3.5 |
| $K_{D_{xy}}$ | 4 |
| $K_{U_\psi}$ | 110 |
| $K_{P_\psi}$ | 66 |
| $K_{I_\psi}$ | 4.4 |
| $K_{D_\psi}$ | 5.0 |

All of these gains were then set and used on the experimental reference trajectory decribed. The ultimate gains were tweaked manually to arrive at the final set. Manually tweaking was necessary to eliminate any marginally stable activity. These final gains are specified in Table IV. The longest oscillation period, $P_U$ of both motion types was found to be about 0.6 s. Evidently, there is a large stable gain region. This gain tuning process cannot be claimed to yield optimal results, however, the values

established satisfy the two most important requirements of control gain tuning:

1. Stable closed loop response
2. The nominal system's closed loop response comfortably meets specifications for simple commanded motion

## C. Results

The PID experiments were run identical to the PD experiments before, so a direct comparison could be made. Ten consecutive experiments were run at each of the same three Kinematic Workspace Coefficients. The maximum absolute error for each run was then averaged over the ten run collection. Figures 14 through 17 summarize the errors seen in postion, velocity, orientation, and angular velocity. Once again, the position and velocity errors represent the magnitude of error seen in both the $x$ and $y$ directions. The PID mean position error shown in Fig. 14 is nearly one-third of the mean error experienced with the PD controller. This same trend is witnessed with the mean orientation error in Fig. 16. The mean velocity and angular velocity errors produced with the PID controller are very close to those recorded using the PD controller in Figures 15 and 17, respectively. The PID controller error in velocity is actually slightly worse at the maximum Kinematic Workspace Coefficient of 1.0. Given how close these PID velocity level errors are to the PD errors, it's clear the advantages from the decreased position level error outweigh what fidelity may be lost at the velocity level. It is important to note again that target errors were never specified for translational and angular velocity tracking. Therefore, these errors were not a priority during the tuning processes.

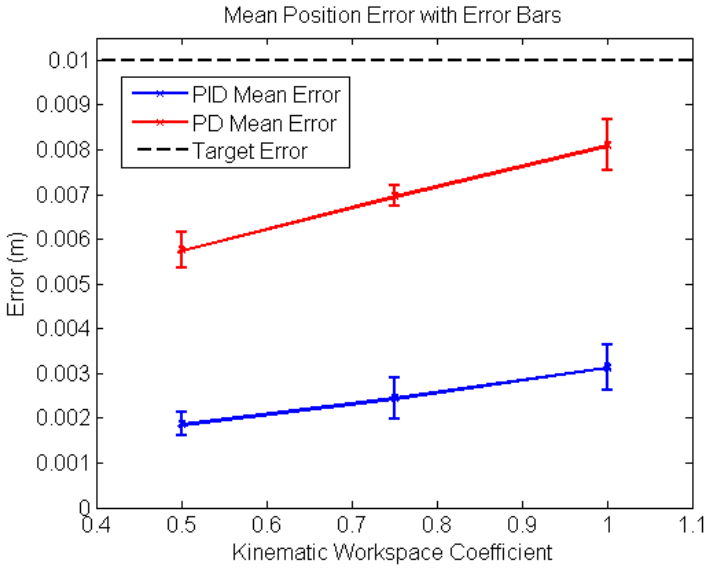


Fig. 14. Mean Maximum PD and PID Position Errors

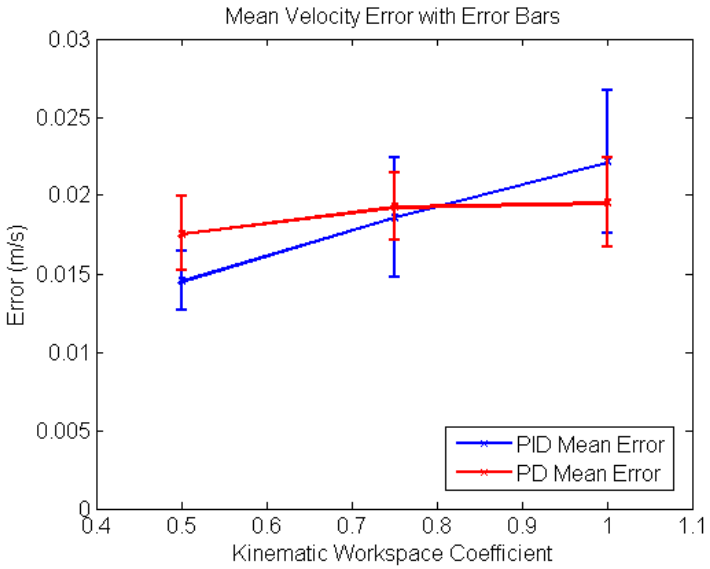


Fig. 15. Mean Maximum PD and PID Velocity Errors

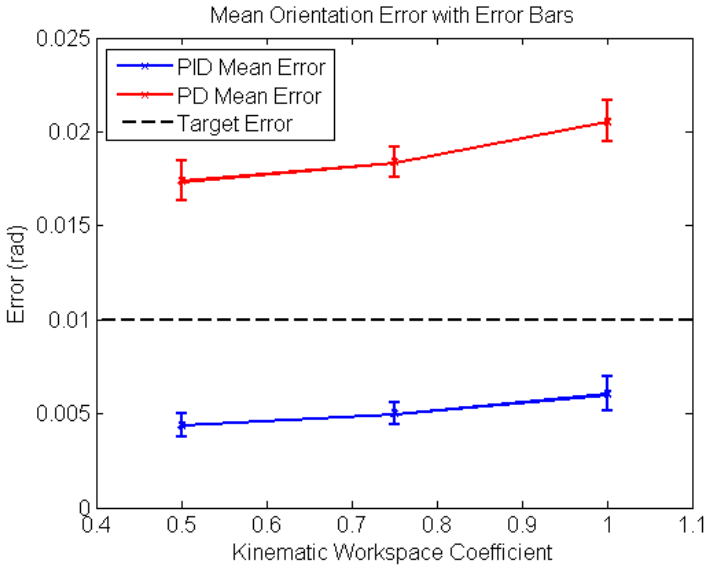


Fig. 16. Mean Maximum PD and PID Orientation Errors

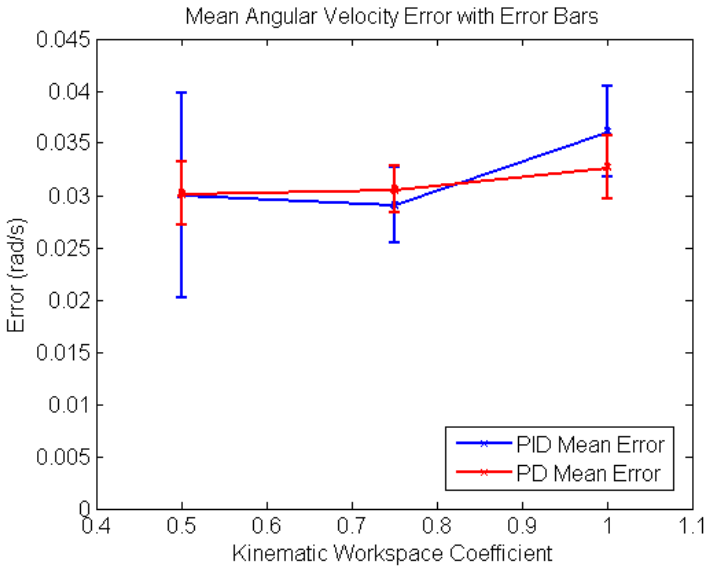


Fig. 17. Mean Maximum PD and PID Angular Velocity Errors

# CHAPTER VII

# FREQUENCY ANALYSIS

One of HOMER's most interesting characteristics is that it incorporates two very different systems with unique advantages and disadvantages into a single system to produce an unmatched, high fidelity ground-based simulation solution. One of the advantages of the Stewart Platform is its ability to replicate high frequency motion, up to 20 Hz. It cannot however, complete large translational or rotational trajectories. Conversely, the base is capable of these large planar motions but is unable to track high frequency trajectories. To get a better idea of the base's closed loop bandwidth, it was beneficial to perform a frequency analysis to determine the limits of base performance.

## A. Method

Once again, the frequency study considered each type of motion independently. To do this, a sinusoidal component was added to each of the simple trajectories used for the PID tuning process. A nominal KWC of 0.75 was selected. When the trajectory reached the specified constant velocity, the sinusoidal component was added. This sinusoidal component, present in the position, velocity, and acceleration profiles, contained a frequency, $f$, and an amplitude, $A$. The angular frequency, $\omega$, is defined by $\omega = 2\pi f$. As an example, the equations used to build the oscillation portion of the reference trajectory are found in Eqn. (7.1) where $x_r$ represents the commanded trajectory and $x_n$ represents the underlying simple, nominal trajectory. The underlying reference trajectory is a constant velocity, straight line motion, but includes the initial two second acceleration phase.

$$
\begin{aligned}
x_r &= x_n - A\cos(\omega t) + A \\
\dot{x}_r &= \dot{x}_n + A\omega \sin(\omega t) \\
\ddot{x}_r &= \ddot{x}_n + A\omega^2 \cos(\omega t)
\end{aligned} \tag{7.1}
$$

The frequency and amplitude values were varied over a specified envelope in an attempt to examine the tracking bandwith of the base. Because certain combinations of frequencies and amplitudes exceeded the specified workspace of the base robot, combinations were chosen that did not violate the maximum velocity of the base. If any of these combinations then exceeded the acceleration limits, the acceleration profile was simply truncated at the robot's physical capabilities. This was done because it was observed that commanded motions that did not violate the velocity or acceleration limits did not produce any interesting results. An example of a standard reference trajectory is shown in Fig. 18 while an example of a truncated reference trajectory is shown in Fig. 19.

## B. Results

Each of the frequency and amplitude combinations were run five consecutive times on the hardware to produce root-mean-squared error data based on the maximum error measured for each run. While this is a very small sample, these repeat experiments let us evaluate the repeatability and stability of the statistics. First, a zero amplitude case was used to determine the baseline error for tracking the underlying reference motion. Next, the boundary cases were found which were defined by the lowest combination producing marginally stable motion or position level error which did not meet the target error specifications. Finally, experiments were run at four frequencies

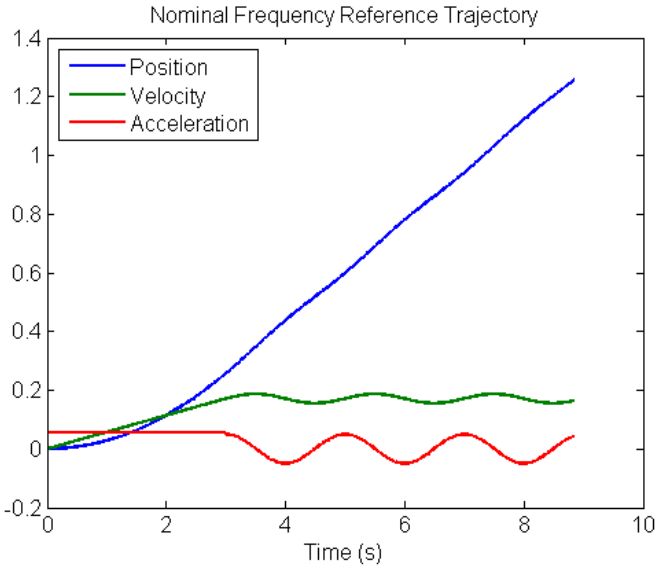


Fig. 18. X-direction Reference Trajectory with f = 0.5 Hz and A = 0.005

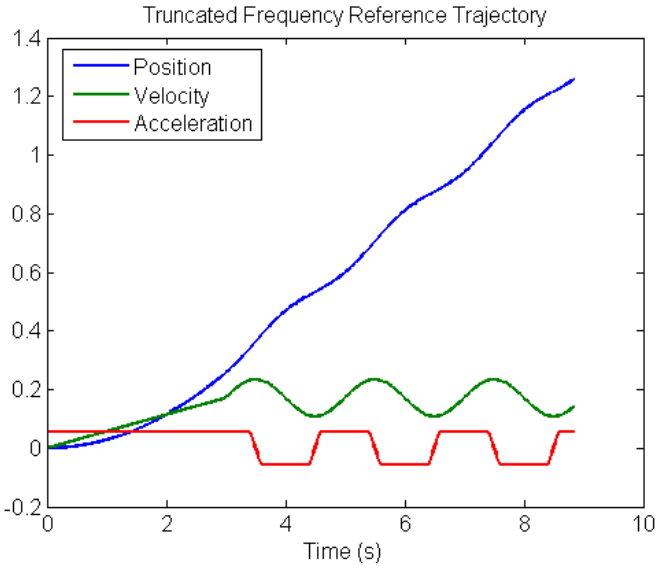


Fig. 19. X-direction Reference Trajectory with f = 0.5 Hz and A = 0.02

for four different amplitudes within the mentioned boundary cases. The plots seen in Figs. 20 and 21 summarize the frequency response analysis of HOMER's base. The error was computed using a root-mean-square (RMS) computation for five consecutive runs.

The translational frequency analysis trend displayed in Fig. 20 is predictably interesting. It's apparent that as the frequency is increased for a given amplitude, the tracking error increases. And, as expected, at a specificed frequency, the error also increases with an increase in amplitude. A similar trend can be seen in Fig. 21 for the rotational data. For an amplitude of 0.02 however, the error trend seemed to be better than higher amplitudes at lower frequencies. It then became rapidly increasing around 0.7 Hz. This anomaly may be attributed to the inconsistencies that arise from the acceleration truncation. Even though the original sinusoidal components remain consistent differentially, the truncation of the acceleration reference trajectory provides the controller with position and velocity trajectories that are impossible based on the acceleration trajectory. A solution to this issue would involve truncating the acceleration trajectory, if necessary, and then integrating to arrive at consistent velocity and position trajectories. Some preliminary work has been done related to this and it is possible to generate closed form solutions for the velocity and position based on a truncated acceleration.

These trends were predicted during the design process and illustrate the need for the Stewart Platform to perform high frequency motion. This analysis also gives us a better understanding of the tracking error that can be expected for a given reference trajectory containing harmonic motions.

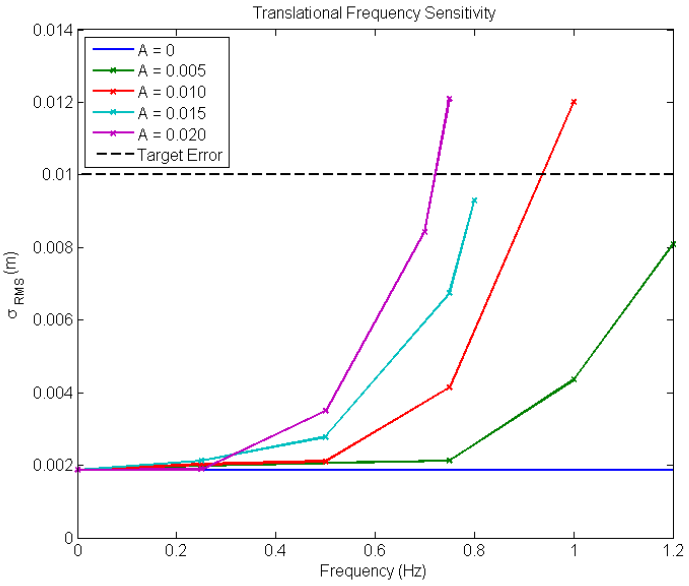


Fig. 20. RMS Error for Translational Bandwidth Experiments

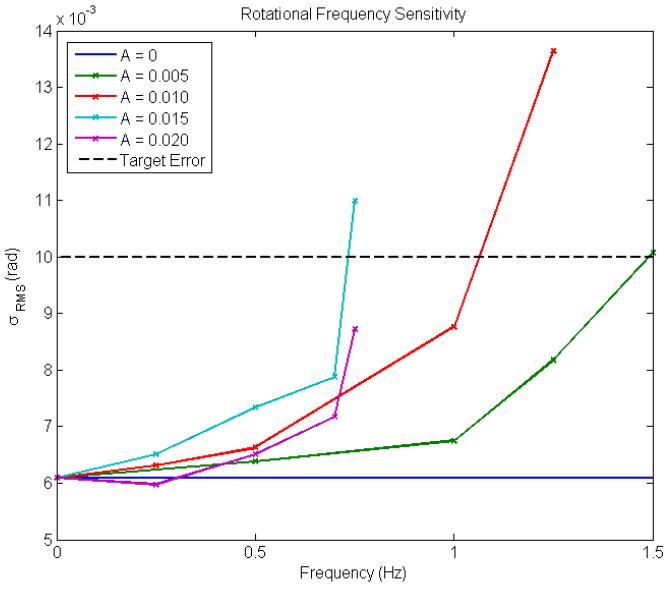


Fig. 21. RMS Error for Rotational Bandwidth Experiments

# CHAPTER VIII

# CONCLUSIONS

## A. Summary

HOMER's base provides an interesting control problem where only a subset of the coordinates defining the system state require stable reference tracking. Because of this property, it's possible to partition the dynamics in such a way that the remaining coordinates are left to ensure stable tracking of the specified reference trajectory. The reference trajectories tested in simulation and hardware were designed using the maximum velocity and acceleration hardware limitations to give a worst case scenario in terms of how aggressive a specified maneuver may be.

After reviewing the computer based simulation results shown in Figs. 5 and 6 it's clear that the controller tracks the reference maneuver quite well when simulated mass and moment of inertia errors approach +/-20% and twice the expected noise is introduced to the measurement feedback. However, once simulated latency is introduced into the system, the controller overcommands when the actual mass and moments of inertia of the system are less than the estimated values. These observations suggest that until the actual latency of a system can be characterized, it is best to underestimate the mass and moments of inertia.

We were able to succesfully trap the specified target translational position target error for each of the Kinematic Workspace Coefficients with the tuned PD controller presented in Ch. III. However, the orientation error experienced was greater than the desired value. An integral term was then added to compensate for constant disturbances such as the effects of a non-flat floor and frictions present in the motors and gear box. The target error values for translational and rotational position were

successfully trapped for all Kinematic Workspace Coefficients using the PID feedback controller presented in Ch. VI.

Finally, a frequency analysis was performed to characterize the bandwidth of HOMER's base. A sinusoidal component was added to each of the position, velocity, and acceleration profiles containing combinations of frequencies and amplitudes. Experiments with different combinations revealed the trends in the tracking error as a function of amplitude and sinusoidal fequency to perturbations added to the ideal trajectory. These trends provide levels of error a user may expect given the amplitude and frequency of simple harmonic perturbations in the desired trajectory.

## B. Future Work

Even though a minimum-norm approach is used to compute the required torques to effectively track a reference motion, it is suspected that the casters (and wheels) may be working against each other. A new control derivation is currently under development using a Newton's second law approach. If considering the desired motion of the main body, a minimum-norm solution is applied to compute the required forces and accelerations at each of the three pivot points. These forces and accelerations can then be mapped to required wheel torques using the caster geometry and the no-sideslip constraint. By applying the minimum-norm on the rigid base, it should be possible to eliminate any "fighting" that may or may not exist between the casters.

This second control derivation method truly captures the essence of the cooperative nature of the three casters. One drawback includes the need for the caster angular accelerations to be computed. Additionally, loads cells could be added to measure the forces between the main body and each caster. Any forces working against each other could then be eliminated or, at the very least, minimized using

adaptation techniques.

The work presented in this thesis represents the development and experimental verification of a controller implemented for the 3-DOF motion of HOMER's base. Next, a second controller will be integrated with the Stewart Platform to give HOMER the full 6-DOF motion capabilities needed for true proximity operations simulations. Additional inertial acceleration and velocity measurements of the base need to be incorporated into both the HOMER and Stewart platform controllers. Utilizing the out-of-plane motion and higher bandwidth of the Stewart platform, we anticipate reducing the target tracking errors even further and allow for sub-millimeter 6-DOF tracking of specified reference trajectories that fall within the bandwidth capabilities of the entire HOMER simulation platform.

Futhermore, an effort needs to be made to reduce the tracking error at the velocity level. During the design stages of HOMER, it was assumed that if the position error was within the target range while operating at 50 Hz, the velocity level error is likely within reason. This notion, however, does not consider higher frequencies induced by high-gain controllers to effectively track the specified position reference trajectory.

Finally, once the Stewart Platform is integrated, the high and low frequency motions of a trajectory will need to be separated in such a way that the base can ignore the frequencies that reside outside of its bandwidth. These higher frequncy motions will then become the responsibility of the Stewart Platform.

# REFERENCES

[1] C. Moody, "Homer hubble," Accessed July 10, 2010: http://www.flickr.com/photos/clarkmoody/4794177016/.

[2] J. L. Schwartz, M. A. Peck, , and C. D. Hall, "Historical review of air-bearing spacecraft simulators," *AIAA Journal of Guidance, Control and Dynamics*, vol. 26, no. 4, pp. 513–522, 2003.

[3] S. Nolet, E. Kong, and D. Miller, "Autonomous docking algorithm development and experimentation using the spheres testbed," in *SPIE Defense and Security Symposium*, Orlando, FL, April 2004.

[4] B. Kim, E. Velenis, P. Kriengsiri, , and P. Tsiotras, "Designing a low-cost spacecraft simulator," *IEEE Control Systems Magazine*, vol. 23, pp. 26–37, August 2003.

[5] Monda, M. J., and H. Schaub, "Hardware simulation of relative navigation using visual sensor information," in *Proceedings of the AIAA Guidance, Navigation and Control Conference*, San Francisco, CA, August 2005.

[6] G. Creamer, F. Pipitone, C. Gilbreath, D. Bird, , and S. Hollander, "Nrl technologies for autonomous inter-spacecraft rendezvous and proximity operations," in *Proceedings of the John L. Junkins Astrodynamics Symposium, AAS/AIAA Space Flight Mechanics Meeting*, College Station, TX, May 2003.

[7] F. D. Roe, D. W. Mitchell, B. M. Linner, and D. L. Kelley, "Simulation techniques for avionics systems - an introduction to a world class facility," in *Proceedings of the AIAA Flight Simulation Technologies Conference*, San Diego, CA, July 1996.

[8] J. Davis, J. Doebbler, K. Daugherty, J. Junkins, and J. Valasek, "Aerospace vehicle motion emulation using omni-directional mobile platform," in *Proceedings of AIAA Guidance, Navigation, and Control Conference*, Hilton Head, SC, August 2007.

[9] X. Bai, J. J. Davis, J. Doebbler, J. Turner, and J. L. Junkins, "Dynamics, control and simulation of a mobile robotics system for 6-dof motion emulation," in *World Congress on Engineering and Computer Science*, San Francisco, CA, October 2007.

[10] H. Schaub and J. L. Junkins, *Analytical Mechanics of Space Systems*, AIAA Education Series, Reston, VA, 2003.

[11] J.G. Ziegler and N.B. Nichols, "Optimum settings for automatic controllers," *Transactions of the ASME*, vol. 64, pp. 759–767, November 1942.

# VITA

Kurt Dale Aures-Cavalieri received his B.S. in Aerospace Engineering and Mechanical Engineering from The State University of New York at Buffalo. He recently completed his M.S. in Aerospace Engineering at Texas A&M University while working under the supervision of Professors John E. Hurtado and John L. Junkins. His research interests are in the areas of robotics, hierarchical control, and control using constraint violation. He will be advancing to the Ph.D. program at Texas A&M University and continue conducting research at the Land, Air, and Space Robotics Laboratory. Kurt can be reached at:

Kurt Dale Aures-Cavalieri

Texas A&M University

Department of Aerospace Engineering

701 H.R. Bright Building - Ross Street

TAMU 3141

College Station, TX 77843-3141